k · p parametrization and linear and circular dichroism in strained monolayer (Janus) transition metal dichalcogenides from first-principles

$\mathbf{k \cdot p}$ Parametrization and Linear and Circular Dichroism in Strained Monolayer (Janus) Transition Metal Dichalcogenides from First-Principles

Yağmur Aksu Korkmaz,[*,†] Ceyhun Bulutay,[*,†] and Cem Sevik[*,‡,¶]

†*Department of Physics, Bilkent University, 06800, Ankara, Turkey*

‡*Department of Mechanical Engineering, Faculty of Engineering, Eskisehir Technical University, 26555, Eskişehir, Turkey;*

¶*Department of Physics, University of Antwerp, Groenenborgerlaan 171, 2020 Antwerp, Belgium;*

E-mail: yaksu@fen.bilkent.edu.tr; bulutay@fen.bilkent.edu.tr; csevik@eskisehir.edu.tr

Abstract

Semiconductor monolayer transition metal dichalcogenides (TMDs) have brought a new paradigm by introducing optically addressable valley degree of freedom. Concomitantly, their high flexibility constitutes a unique platform that links optics to mechanics via valleytronics. With the intention to expedite the research in this direction, we investigated ten TMDs, namely MoS_2, $MoSe_2$, $MoTe_2$, WS_2, WSe_2, WTe_2, MoSSe, MoSeTe, WSSe, and WSeTe, which particularly includes their so-called janus types (JTMDs). First, we obtained their electronic band structures using regular and hybrid density functional theory (DFT) calculations in the presence of the spin-orbit coupling, and biaxial or uniaxial strain. Our DFT results indicated that against the expectations

based on their reported piezoelectric behavior, JTMDs typically interpolated between the standard band properties of the constituent TMDs without producing a novel feature. Next, by fitting to our DFT data we generated both spinless and spinful $\mathbf{k} \cdot \mathbf{p}$ parameter sets which are quite accurate over the K valley where the optical activity occurs. As an important application of this parametrization, we considered the circular and linear dichroism under strain. Among the studied (J)TMDs, WTe_2 stood out with its largest linear dichroism under uniaxial strain because of its narrower band gap and large K valley uniaxial deformation potential. This led us to suggest WTe_2 monolayer membranes for optical polarization-based strain measurements, or conversely, as strain tunable optical polarizers.

Introduction

Transition metal dichalcogenides, MX_2 with the structure consisting of one layer of M atoms (transition metals such as Mo, W, etc.) sandwiched between two layers of X atoms (chalcogen, S, Se, or Te) have been studied extensively due to their intriguing physical properties.[1] In the first place, being mostly semiconducting materials, they have attracted significant interest potentially as transistors[2,3] and optical emitters.[4] Further extensive investigations have revealed novel applications such as valleytronics,[5,6] piezotronics,[7] phototransistors, and photodetectors.[8] On the material growth, the complex TMD structures consisting of chalcogen layers formed with different atoms (MX_2), dubbed janus TMD (JTMD)[9,10] (MXX') have been experimentally realized with a chemical vapor deposition technique.[11,12] This important development, first practiced with the sulfurization or selenization of MoS_2/Se_2, multiplies alternative materials within this family and promotes piezoelectric behavior by breaking the mirror symmetry in the out-of plane direction.[13] In recent experimental studies, also their two-layer hetero compounds, $MoSSe/MoS_2$, MoSSe/WSSe, and WSSe/MoSSe have been reported along with the use of strain as a control mechanism on dynamical and optical properties of these materials.[14–16]

Naturally accompanying the experimental progress, first-principles studies have considered a vast number of (J)TMD crystals and unveiled further two-dimensional TMDs with the unique optical,[17] transport,[18–20] piezoelectric,[13,21] and flexoelectric[22] physical properties. Moreover, the use of these materials in future technological applications such as optoelectronics,[23–25] valleytronics,[26–28] solar power harvesting,[29–33] gas sensing,[34–37] and water splitting[38–43] have been demonstrated.

In addition to these exciting uses for (J)TMDs, two other directions which hold promise, but are so far overlooked, are the high-precision polarization photodetection and optical polarization-based strain measurements. The polarization is one of the characteristic properties of an electromagnetic wave just like its wavelength. Probing this feature of radiation requires materials showing so-called dichroic behavior, where there is preferential absorption of a resonant photon according to its polarization. In the case of TMDs, very early on they were discovered to be optically chiral, meaning, they display a strong valley-selective circular dichroism (CD), arising from broken inversion (C_3) symmetry.[5,6,44–47] This is accompanied by a nonzero Berry curvature[6,48] which leads to other interesting physics such as the valley Zeeman effect.[49,50] From the application standpoint of CD in TMDs, one proposal is designing polarization-sensitive meta-materials for imaging devices and display technologies.[51] As opposed to CD, the linear dichroism (LD) discriminates the electromagnetic absorption for two orthogonal linear polarizations. Yet, a pristine monolayer TMD because of the particular in-plane symmetry does not show LD at the K-point where there occurs the conduction and valence band extrema. Having said this, under uniaxial strain the D_{3h} point-group symmetry of monolayer TMDs is lowered to C_{2v} which allows for LD at the K point, thus constituting a candidate platform for high performance polarization photodetection.[52]

As mentioned above, much of the progress in this field is enabled by first-principles calculations, predominantly using the density functional theory (DFT) technique.[53–55] Here, one should note that these are quite demanding because of their excessive computational budget, especially for highly accurate band gap in the presence of symmetry-lowering strain

and spin-orbit coupling. On the other extreme of the computational complexity scale with respect to DFT, there is the so-called $\mathbf{k}\cdot\mathbf{p}$ method which offers the simplest alternative that can describe most of the electronic and optical properties,[56] though, its performance crucially depends on its parametrization. There are a number of $\mathbf{k}\cdot\mathbf{p}$ parameter sets for monolayer TMDs,[48,57–61] but to the best of our knowledge, none so far for JTMDs.

In this work, choosing ten semiconductor monolayer (J)TMDs consisting of MoS_2, $MoSe_2$, $MoTe_2$, WS_2, WSe_2, WTe_2, MoSSe, MoSeTe, WSSe, and WSeTe, we study several key electronic and optical properties. First, we obtained their electronic band structures using regular and hybrid DFT calculations, including the spin-orbit coupling. Taking into account strain engineering of (J)TMDs,[62] we intently considered the effects of biaxial and uniaxial strain, that yield the corresponding electronic deformation potentials of the K valley. From our DFT results, we extracted both spinless and spinful $\mathbf{k}\cdot\mathbf{p}$ parameter sets. The electron-hole asymmetry, trigonal warping, cubic,[57,58] and the strain[61] terms of the Hamiltonian are included, so that a faithful agreement with the DFT data is attained over the K valley. Finally, using this $\mathbf{k}\cdot\mathbf{p}$ electronic structure we investigated the CD and LD properties of these materials. Here, our main finding is that WTe_2 develops the largest LD under uniaxial strain, the reason being both its narrower band gap and large K valley uniaxial deformation potential. Another noteworthy point is that, unlike their enhanced piezoelectric behavior,[13] for the properties considered in this work our results did not show a distinct feature of JTMDs in comparison to constituent TMDs, in other words, the values of MSSe typically interpolate between the MS_2 and MSe_2. Such characteristics for JTMDs is somewhat expected in this context, as they mainly break the mirror symmetry perpendicular to the atomic plane,[13] whereas the effects like CD stem from the in-plane 3-fold rotational symmetry.[46]

An important remark is that for all the (J)TMDs considered in this work, the amount of strain exerted is limited to values such that the materials are assured to remain a direct band gap.[59] Indirect band gap materials are undesirable because of their orders of magnitude weaker optical transitions than direct gap counterparts.[63] Nevertheless, in principle the $\mathbf{k}\cdot\mathbf{p}$

technique offered in this work can be extended to indirect band gap (J)TMDs or strain regimes. This amounts to switching from a specific valley, say K, to the full zone $\mathbf{k} \cdot \mathbf{p}$ approach.[64] The price to be paid is the need for much higher number of bands, for instance, 15 for the spinless case, whereas 4- and 8-band approaches were shown to fail.[65] One inevitable drawback of the increase of the number of bands is the proliferation of the corresponding $\mathbf{k} \cdot \mathbf{p}$ parameters.

The organization of the paper is as follows. First, we describe our computational and theoretical methods, namely, DFT, $\mathbf{k} \cdot \mathbf{p}$, and dichroism formulations. Then, we present detailed DFT electronic structure results for unstrained and strained (J)TMDs. These are then used to extract the $\mathbf{k} \cdot \mathbf{p}$ parameters including strain and spin-orbit effects. On the basis of this parametrization, we obtain CD and LD when these (J)TMDs are subjected to biaxial, uniaxial and shear strain. Finally, we summarize our main findings. Extensive additional results for each section are available in the Supporting Information.

Methods

First-Principles Calculations

The DFT calculations were performed using the Vienna Ab Initio Simulation Package (VASP).[53] The projector augmented wave[54] type Perdew–Burke–Ernzerhof (PBE)[66] exchange-correlation functionals based on Generalized Gradient Approximation were used. Since PBE functional underestimates the band gap of the semiconductor materials, the Heyd-Scuseria-Ernzerhof (HSE)[55] approach was employed over the PBE calculations in order to predict the results comparable with the experiments. Due to the strong spin-orbit coupling (SOC) previously predicted for TMDs,[45] it was specifically included in both PBE and HSE calculations. The plane wave energy cutoff as 500 eV was used considering the desired accuracy in the band structures to be used in $\mathbf{k} \cdot \mathbf{p}$ parameter fitting. The Brillouin zone integration (k-point sampling) scheme was chosen as Monkhorst-Pack and the corresponding values were set to

36×36×1 and 15×15×1 for PBE and HSE calculations, respectively. The convergence criteria for total energy and ionic forces were chosen as 1×10^{-7} and 0.0001 eVÅ^{-1}. Atomic structure of (J)TMD and their reciprocal space high symmetry points for hexagonal and tetragonal crystal structures are seen in Figure 1 a, b.

$\mathbf{k}\cdot\mathbf{p}$ Theory

The $\mathbf{k}\cdot\mathbf{p}$ is an empirical band structure method using a discrete set of Bloch states, most commonly chosen at the bandedges, as the basis functions.[56] It offers a simple low-energy Hamiltonian which takes into account interband and spin-orbit couplings as well as perturbations such as strain. For the spin-orbit coupling we used the wave vector independent and diagonal in spin-space approximations.[57,58] Thus, this leads to a decoupled two-band $\mathbf{k}\cdot\mathbf{p}$ Hamiltonians for each spin label s, which we shall denote using a superscript as $\mathcal{H}^s$. We also provide spinless $\mathbf{k}\cdot\mathbf{p}$ parameters, in which case this label in the expressions should be ignored. Throughout this work we shall assume the $+K$ valley without loss of generality, while the expressions for the $-K$ valley can be obtained by a time-reversal operation (orbital part conjugation and spin label flip).[67]

For two-dimensional materials the starting point of the Hamiltonian is the electron-hole symmetric part;[67] choosing the $+K$ valley as the origin for (k_x, k_y) axes it takes the form

$$\mathcal{H}^s_{\text{symm}} = \frac{f_1^s}{2}\sigma_z + f_2^s a(k_x\sigma_x + k_y\sigma_y)\,, \tag{1}$$

where a is the lattice constant of the crystal, σ_i's are the Cartesian components of the Pauli matrix, f_1^s is the energy gap and f_2^s is defined as the velocity in the Dirac equation.[61] This sets the correct band gap but with symmetric dispersion for the conduction and valence bands. Note that in our choice of basis ordering the conduction and valence bandedge vectors correspond to $(1\quad 0)^T$ and $(0\quad 1)^T$, respectively.[61] For TMDs additional contributions are crucial,[57,58] namely, the asymmetry term which breaks the symmetry between the conduction

and the valence bands

$$\mathcal{H}^s_{\text{asym}} = k^2 \begin{pmatrix} \beta^s & 0 \\ 0 & \alpha^s \end{pmatrix}, \tag{2}$$

the term that introduces trigonal warping to otherwise isotropic energy dispersion

$$\mathcal{H}^s_{\text{TW}} = \kappa^s \begin{pmatrix} 0 & k_+^2 \\ k_-^2 & 0 \end{pmatrix}, \tag{3}$$

and the cubic term that enables a better fit to DFT results over a larger portion of the K valley

$$\mathcal{H}^s_{\text{cub}} = \frac{\eta^s}{2} k^2 \begin{pmatrix} 0 & k_- \\ k_+ & 0 \end{pmatrix}, \tag{4}$$

where $k_\pm \equiv k_x \pm i k_y$. Additionally, strain can be accommodated up to linear in mechanical perturbation as[61]

$$\mathcal{H}_\varepsilon = f_4(\varepsilon_{xx} + \varepsilon_{yy})\sigma_z + f_5 \left[(\varepsilon_{xx} - \varepsilon_{yy})\sigma_x - 2\varepsilon_{xy}\sigma_y\right]. \tag{5}$$

Note that we considered these two deformation potentials, f_4 and f_5 as spin independent. Thus, the overall $\mathbf{k} \cdot \mathbf{p}$ Hamiltonian to be fitted to the DFT band structure becomes

$$\mathcal{H}^s = \mathcal{H}^s_{\text{symm}} + \mathcal{H}^s_{\text{asym}} + \mathcal{H}^s_{\text{TW}} + \mathcal{H}^s_{\text{cub}} + \mathcal{H}_\varepsilon. \tag{6}$$

As described above each term in this Hamiltonian has a well defined and distinct purpose. To preserve this hierarchy, the parameter fittings are done sequentially, starting with the symmetric (massive Dirac Fermion) part which we explain below.

Parameter Fitting Expressions

The parameters, f_1^s, f_2^s, α^s, and β^s were extracted by fitting to DFT results using successively the following expressions

$$f_1^s = E_{\rm CB}^s - E_{\rm VB}^s, \tag{7}$$

$$f_2^s = \frac{\hbar}{a}\sqrt{\frac{f_1^s}{m_c^{*s} - m_v^{*s}}}, \tag{8}$$

$$\alpha^s = \frac{\hbar^2}{2m_v^{*s}} + \frac{(f_2^s a)^2}{f_1^s}, \tag{9}$$

$$\beta^s = \frac{\hbar^2}{2m_c^{*s}} - \frac{(f_2^s a)^2}{f_1^s} \tag{10}$$

where the DFT values of $E_{\rm CB}^s$ ($E_{\rm VB}^s$) and $m_c^{*s} > 0$ ($m_v^{*s} < 0$) for the conduction (valence) bandedge energy and effective mass for the spin component s were used. We defined the spin splitting for conduction band (CB) as $\Delta_{\rm CB} = E_{\rm CB}^{\downarrow} - E_{\rm CB}^{\uparrow}$ and the valence band (VB) as $\Delta_{\rm VB} = E_{\rm VB}^{\downarrow} - E_{\rm VB}^{\uparrow}$. Therefore, as a crosscheck, in terms of spin splittings we also have the relation $f_1^{\uparrow} = f_1^{\downarrow} - \Delta_{\rm CB}^{\rm SO} + \Delta_{\rm VB}^{\rm SO}$. We fixed the κ^s parameter by fitting the isoenergy contours to the DFT values for each spin component to ensure trigonal warping. For the agreement with DFT bands at a larger scale, the η^s parameter was employed.[48,57,58]

The f_4 was fitted to the strain-dependent DFT band gap value,

$$E_g = f_1 + 2f_4(\varepsilon_{xx} + \varepsilon_{yy})\,. \tag{11}$$

Similarly, f_5 was extracted by using

$$\Delta k_{x0} = \frac{f_5}{f_2 a}(\varepsilon_{xx} - \varepsilon_{yy}), \tag{12}$$

where Δk_{x0} represents the shift in band extreme under uniaxial strain, predicted by DFT.

Dichroism within $\mathbf{k}\cdot\mathbf{p}$ Hamiltonian

For a direct interband transition under a light polarized along the $\hat{\epsilon}$ unit vector direction, the momentum matrix element component is

$$P_{\epsilon}^{cv}(\mathbf{k}) \equiv u_c^s(\mathbf{k})\hat{\epsilon}\cdot\mathbf{p}\, u_v^s(\mathbf{k}), \tag{13}$$

which can be written in a more convenient way for $\mathbf{k}\cdot\mathbf{p}$ as[67]

$$P_{\epsilon}^{cv}(\mathbf{k}) = \frac{m_0}{\hbar}\left\langle u_c^s\middle|\frac{\partial\mathcal{H}(\mathbf{k})}{\partial k_\epsilon}\middle|u_v^s\right\rangle. \tag{14}$$

Here, m_0 is the free-electron mass and $|u_{c,v}^s\rangle$ stands for the cell-periodic parts of Bloch states of CB/VB.[67] In the remainder of this subsection, we suppress the spin label s for the sake of notational simplicity.

For the circular polarizations $\hat{\epsilon}_\pm = \mp(\hat{x}\pm i\hat{y})/\sqrt{2}$, the momentum matrix element $\mathbf{p}_\pm = \hat{\epsilon}_\pm\cdot\mathbf{p}$ becomes

$$\mathbf{p}_\pm = \mp\frac{1}{\sqrt{2}}\left(\frac{\partial\mathcal{H}}{\partial k_x}\pm i\frac{\partial\mathcal{H}}{\partial k_y}\right), \tag{15}$$

whereas, for the linear polarizations, $\hat{\epsilon}=\hat{x}$ and $\hat{\epsilon}=\hat{y}$, the operator derivatives are straightforward.

Within the corresponding spin-subspace, any two-band Hamiltonian, as in eq. (6), can be written as a superposition of Pauli matrices σ_i, $i=0$ to 3 with $\sigma_0=1$, as $\mathcal{H}=h_i\sigma_i$, where summation over repeated index i is implied, giving the explicit form[68]

$$\mathcal{H} = \begin{pmatrix} h_0+h_3 & h_1-ih_2 \\ h_1+ih_2 & h_0-h_3 \end{pmatrix}. \tag{16}$$

The corresponding eigenvectors in terms of $r\equiv\frac{h_1+ih_2}{\overline{h}+h_3}$, $\overline{h}\equiv\sqrt{h_1^2+h_2^2+h_3^2}$, can be expressed

as

$$|u_c\rangle = \frac{1}{\sqrt{1+|r|^2}} \begin{pmatrix} 1 \\ r \end{pmatrix}, \tag{17}$$

$$|u_v\rangle = \frac{1}{\sqrt{1+|r|^2}} \begin{pmatrix} -r^* \\ 1 \end{pmatrix}. \tag{18}$$

Likewise, if we express $\partial_\epsilon \mathcal{H} = d_i^\epsilon \sigma_i$, for Hamiltonian derivatives along $\hat{\epsilon}$ (see the next section for their expressions), the final form of the momentum matrix element becomes

$$P_\epsilon^{cv} = \frac{m_0}{\hbar(1+|r|^2)} \left[-2d_3^\epsilon r^* + d_1^\epsilon \left(1 - r^{*2}\right) - i d_2^\epsilon \left(1 + r^{*2}\right) \right]. \tag{19}$$

Using P_ϵ^{cv}, the $v \to c$ interband absorption dichroism can be quantified in terms of $\mathbf{k}$-resolved degree of optical polarization, under a circular electromagnetic field as[46]

$$\eta_C^{cv}(\mathbf{k}) = \frac{\left|P_+^{cv}(\mathbf{k})\right|^2 - \left|P_-^{cv}(\mathbf{k})\right|^2}{\left|P_+^{cv}(\mathbf{k})\right|^2 + \left|P_-^{cv}(\mathbf{k})\right|^2}, \tag{20}$$

and under a linear polarization

$$\eta_L^{cv}(\mathbf{k}) = \frac{\left|P_x^{cv}(\mathbf{k})\right|^2 - \left|P_y^{cv}(\mathbf{k})\right|^2}{\left|P_x^{cv}(\mathbf{k})\right|^2 + \left|P_y^{cv}(\mathbf{k})\right|^2}. \tag{21}$$

These are numerically computed according to eq. (19) once d_i^ϵ is available.

$\partial\mathcal{H}/\partial k_\epsilon$ Expressions

In this subsection we provide the expressions for d_i^ϵ to be used in eq. (19). For linear polarization components, $\epsilon = x, y$, we obtain

$$\frac{\partial \mathcal{H}_{\rm symm}}{\partial k_\epsilon} = f_2 a\, \sigma_\epsilon, \tag{22}$$

$$\frac{\partial \mathcal{H}_{\rm asym}}{\partial k_\epsilon} = 2k_\epsilon \begin{pmatrix} \beta & 0 \\ 0 & \alpha \end{pmatrix}. \tag{23}$$

In the case of circular polarization, $\epsilon = +, -$, they become

$$\partial_\pm \mathcal{H}_{\rm symm} = \mp\sqrt{2} f_2 a \sigma_\pm, \tag{24}$$

$$\partial_\pm \mathcal{H}_{\rm asym} = -\sqrt{2} k_\mp \begin{pmatrix} \beta & 0 \\ 0 & \alpha \end{pmatrix}, \tag{25}$$

where $\sigma_\pm = (\sigma_x \pm i\sigma_y)/2$.

The remaining derivatives of the Hamiltonian terms are similarly worked out as

$$\partial_x \mathcal{H}_{\rm TW} = 2\kappa \begin{pmatrix} 0 & k_+ \\ k_- & 0 \end{pmatrix}, \tag{26}$$

$$\partial_y \mathcal{H}_{\rm TW} = 2i\kappa \begin{pmatrix} 0 & k_+ \\ -k_- & 0 \end{pmatrix}, \tag{27}$$

$$\partial_+ \mathcal{H}_{\rm TW} = -2\sqrt{2}\kappa \begin{pmatrix} 0 & 0 \\ k_- & 0 \end{pmatrix}, \tag{28}$$

$$\partial_- \mathcal{H}_{\rm TW} = 2\sqrt{2}\kappa \begin{pmatrix} 0 & k_+ \\ 0 & 0 \end{pmatrix}, \tag{29}$$

$$\partial_x \mathcal{H}_{\rm cub} = \frac{\eta}{2} \begin{pmatrix} 0 & 4k_x^2 - k_+^2 \\ 4k_x^2 - k_-^2 & 0 \end{pmatrix}, \tag{30}$$

$$\partial_y \mathcal{H}_{\rm cub} = i\frac{\eta}{2} \begin{pmatrix} 0 & -4k_y^2 - k_+^2 \\ 4k_y^2 + k_-^2 & 0 \end{pmatrix}, \tag{31}$$

$$\partial_+ \mathcal{H}_{\rm cub} = -\frac{\eta}{\sqrt{2}} \begin{pmatrix} 0 & 2k_+k_- \\ k_+^2 & 0 \end{pmatrix}, \tag{32}$$

$$\partial_- \mathcal{H}_{\rm cub} = \frac{\eta}{2} \begin{pmatrix} 0 & k_-^2 \\ 2k_+k_- & 0 \end{pmatrix}. \tag{33}$$

Approximate Analytical Expressions

If we retain the symmetry and asymmetry terms of the Hamiltonian, that is eqs. 1 and 2, respectively we get the linear polarization matrix elements as

$$P_x^{cv} = \tfrac{m_0}{\hbar(1+|r|^2)} \left[-2k_x(\beta-\alpha)r^* + f_2 a\left(1 - r^{*2}\right)\right], \tag{34}$$

$$P_y^{cv} = \tfrac{m_0}{\hbar(1+|r|^2)} \left[-2k_y(\beta-\alpha)r^* - if_2 a\left(1 + r^{*2}\right)\right]. \tag{35}$$

For the circular polarization, these are

$$P_{+}^{cv} = \frac{\sqrt{2}m_0}{\hbar(1+|r*|^2)}\left[k_{-}(\beta-\alpha)r^{*} - f_2 a\right], \tag{36}$$

$$P_{-}^{cv} = \frac{\sqrt{2}m_0}{\hbar(1+|r*|^2)}\left[k_{+}(\beta-\alpha)r^{*} - f_2 a r^{*2}\right]. \tag{37}$$

For simplified analytical expressions at the expense of some further approximation, we can keep only the contribution from $\mathcal{H}_{\text{symm}}$, in eq. (1). Then, the degree of linear polarization reduces to

$$\eta_L^{cv} = \frac{\left|1-r^{*2}\right|^2 - \left|1+r^{*2}\right|^2}{\left|1-r^{*2}\right|^2 + \left|1+r^{*2}\right|^2} = \frac{2(h_2^2-h_1^2)(h_3+\overline{h})^2}{(h_1^2+h_2^2)^2+(h_3+\overline{h})^4}. \tag{38}$$

As will be later shown, this will shed light in revealing which parameters play a role in enhancing linear polarization dichroism under uniaxial strain. Finally, the same expression for the degree of circular polarization is obtained as

$$\eta_C^{cv} = \frac{1-|r|^4}{1+|r|^4} = \frac{(h_3+\overline{h})^4-(h_1^2+h_2^2)^2}{(h_1^2+h_2^2)^2+(h_3+\overline{h})^4}. \tag{39}$$

Results and Discussion

DFT Results

Our calculated electronic band structures and band gap values for TMD monolayers are in very good agreement with the literature[58] as depicted in the Supporting Information. However, for some JTMD structures our results slightly contradict the available literature.[19,69–71] Figure 2 shows the electronic band structures calculated using PBE and PBE+SOC, where VB maximum (VBM) is set to zero. The materials MoSTe and WSTe are obtained to be indirect band gap materials, whereas the rest were calculated as direct band gap, with both corresponding CBM and VBM being at the K point in the Brillouin zone. The difference between the PBE direct (1.55 eV) and indirect band gap (1.57 eV) values of MoSSe is only

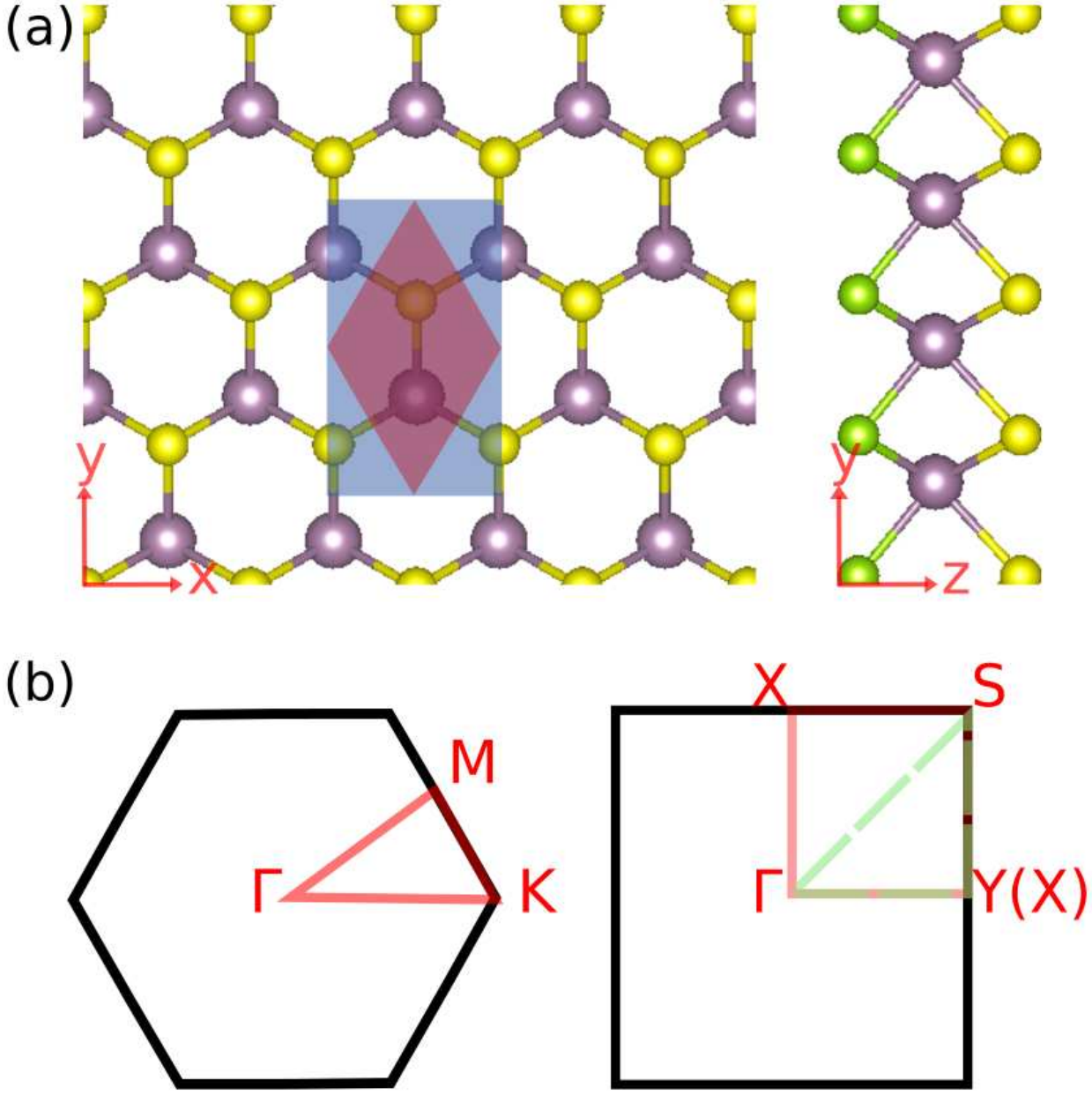

Figure 1: (a) Top and side view of JTMDs. (b) High symmetry points corresponding for hexagonal and orthorhombic (tetragonal) lattice, respectively.

20 meV, but in the PBE+SOC results the direct gap is more clear. In fact, this slight difference somehow clarifies the direct[29,39,72,73] and indirect[19,69–71] band gap result diversity in the literature. Contradicting results exist in the literature also for WSSe, MoSeTe, and WSeTe.[29,39,69,70,73] Considering these differences, we revisited the computations both with and without SOC and reported the band parameters.

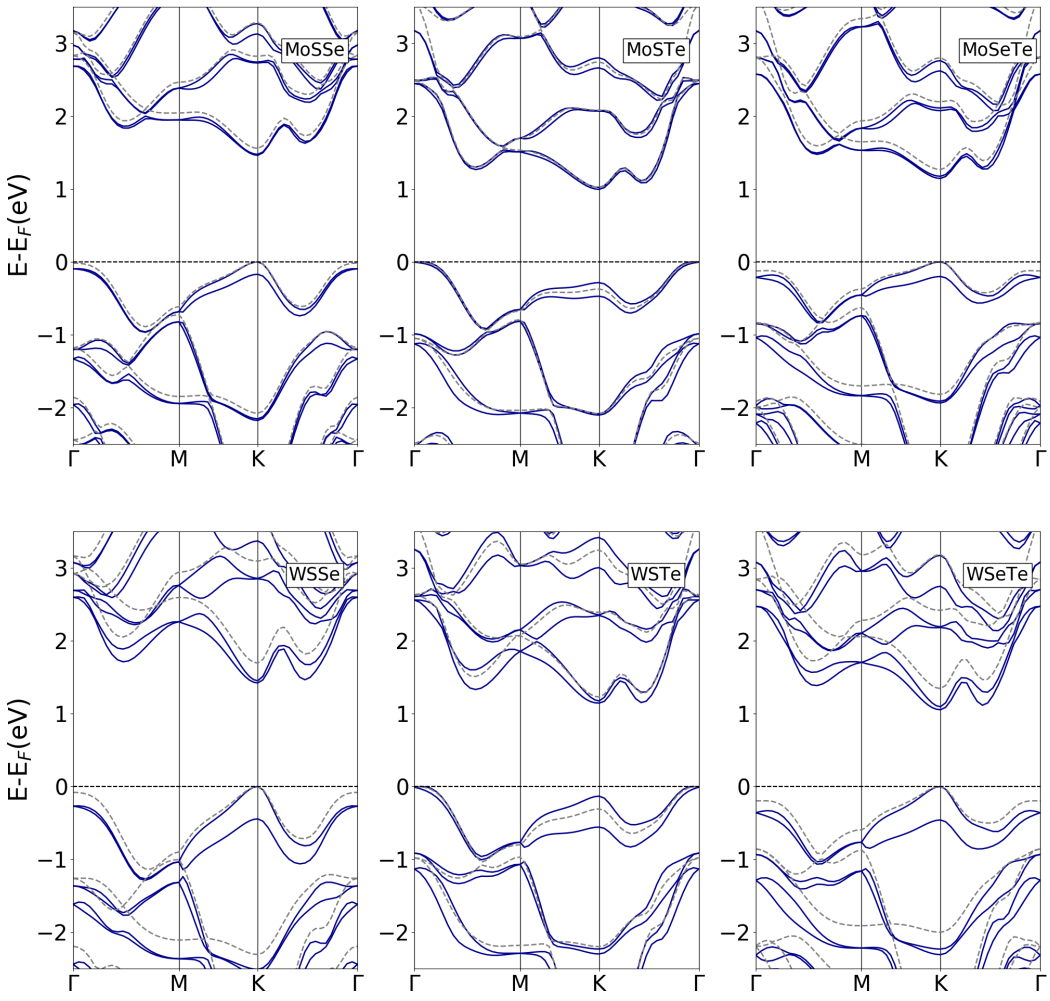

Figure 2: MoXX' and WXX' band structures calculated PBE (gray/dashed) and PBE+SOC (blue/solid).

In Table 1, acquired band gap values for TMDs and JTMDs are presented. For MoX_2 and WX_2 (X=S,Se,Te) monolayers, the calculated band gap decreases when X changes as S→Se→Te which can also be monitored in the band structure plots presented in the Supporting Information. This characteristic behavior is also observed in direct band gap janus structures depicted in Figure 2. Our results clearly reveal that the band gap values of the janus structures can be estimated by the average of corresponding pristine TMD monolayers. For instance, for the band gap value of MoSSe, 1.56 eV is almost equal to the average of the band gap values of MoS_2, 1.66 eV and $MoSe_2$, 1.43 eV. The hybrid DFT calculations adopted on PBE and PBE+SOC computations increase the band gaps around 0.4-0.5 eV but do not alter the mentioned features.

Table 1: Band Gaps Calculated with PBE and HSE Compared with and without SOC[a]

	E_{gap}^{PBE} (eV)	E_{gap}^{HSE} (eV)	$E_{gap}^{PBE+SOC}$ (eV)	$E_{gap}^{HSE+SOC}$ (eV)
MoS_2	1.66	2.13	1.58	2.02
$MoSe_2$	1.43	1.89	1.32	1.72
$MoTe_2$	1.08	1.46	0.94	1.27
WS_2	1.80	2.29	1.54	1.99
WSe_2	1.53	2	1.24	1.64
WTe_2	1.06	1.47	0.74	1.07
MoSSe	1.55	2.01	1.45	1.87
MoSTe	1.01 (I)	1.49 (I)	0.99 (I)	1.45 (I)
MoSeTe	1.28	1.69	1.12	1.50
WSSe	1.68	2.16	1.41	1.84
WSTe	1.24 (I)	1.71 (I)	1.16 (I)	1.62 (I)
WSeTe	1.34	1.78	1.05	1.41

[a] The band gaps refer to KK points for direct materials and ΓK points for indirect materials designated with I (MoSTe and WSTe).

SOC has a notable influence on the electronic structure of JTMDs as predicted in pristine ones.[58] The calculated band gap values are 0.1-0.3 eV and 0.1-0.4 eV lower than the values obtained with PBE and HSE computations without SOC, respectively. However, the direct or indirect nature of the bands is not affected as seen in Figure 2. WX_2 and WXX' materials possess larger valence states SOC splitting values compared with Mo counterparts (the values are almost $2\,\Delta_{MoX_2/MoXX'}$) since they are heavier materials, see Table 2. The hybrid calculations result in larger valence states splitting values, in particular for W-based materials. Overall, the predicted picture with the inclusion of SOC agrees very well with the available literature[58] for

both pristine and janus structures.

Table 2: Splittings in CB and VB Calculated with PBE and HSE[a]

	Δ_{VB}^{PBE} (meV)	Δ_{CB}^{PBE} (meV)	Δ_{VB}^{HSE} (meV)	Δ_{CB}^{HSE} (meV)
MoS_2	150	-30	210	-20
$MoSe_2$	180	-20	280	-40
$MoTe_2$	220	-40	350	-70
WS_2	430	30	550	1
WSe_2	470	30	620	3
WTe_2	490	50	740	2
MoSSe	220	-20	240	-30
MoSTe	200	-30	280	-50
MoSeTe	200	-40	310	-60
WSSe	440	30	580	2
WSTe	420	30	580	1
WSeTe	470	40	630	10

[a] The splittings are calculated at K point for CB and VB, except for MoSTe and WSTe at Γ point for VB. For all splitting calculations $E^{\downarrow}_{CB/VB} - E^{\uparrow}_{CB/VB}$ formula is used.

Strain with DFT Results

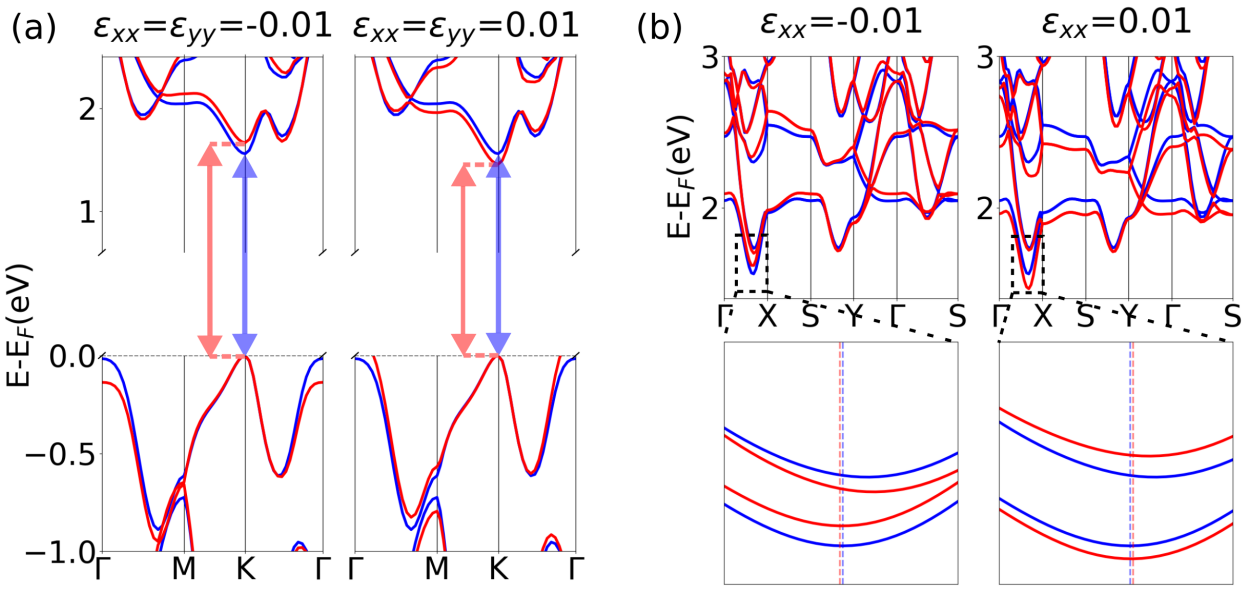

Figure 3: MXX' band structure with (a) biaxial strain (b) uniaxial strain.

In order to investigate circular and linear dichroism effects, $\mathbf{k}\cdot\mathbf{p}$ parametrization also for strained cases is crucial. In this regard, we also generated the desired electronic structure data to fit $\mathbf{k}\cdot\mathbf{p}$ parameters enabling

strain analysis. Therefore, we calculated electronic properties of MXX$'$ (M=Mo,W and X,X'=S,Se,Te) under biaxial ($\varepsilon_{xx} = \varepsilon_{yy} \neq 0$) and uniaxial ($\varepsilon_{xx} \neq 0,\ \varepsilon_{yy} = 0$) compressive and tensile strain from -2% to 2%. Biaxial strain changes the band gap around K point as can be seen in Figure 3a. Using this energy difference, we are able to obtain f_4 parameter by eq. (11). Direct to indirect band gap changes are observed in the electronic band structures, as provided in Figures S2-S5. Since we focused on characterization by $\mathbf{k} \cdot \mathbf{p}$ method around K valley, these features are not considered in the calculations.

Instead of using the hexagonal crystal structure as in the biaxial strain, we switched to the tetragonal structure for ease of applying an uniaxial strain. For the unstrained case, the crystal structure has $a = b \neq c$. However, as the strain is applied, the length of one side changes so that $a \neq b \neq c$, turning the crystal into an orthorhombic structure. Here, we have chosen the crystal path of the orthorhombic structure to compare unstrained and strained systems as in Figure 1.

As a result of uniaxial strain applied along x direction, a shift appears at the k axis for CBM which can be observed in Figure 3b. The inset drawing shows this shift in Cartesian coordinates, and using eq. (12), the f_5 parameter is calculated.

In accordance with the strain results, MoSTe and WSTe have an indirect band gap at ΓK with and without strain. Since we are interested in the change around the K valley, these materials are not going to be considered for $\mathbf{k} \cdot \mathbf{p}$ calculations. For the remaining materials, 1% tensile strain results have been used as they provide the most consistent values. For further details about strain results, we refer to Figures S6-S9 and Tables S3-S5.

Table 3: Spinless $\mathbf{k} \cdot \mathbf{p}$ parameters a (Å) f_1 (eV), f_2 (eV), f_4 (eV), f_5 (eV), α (eV Å^2), β (eV Å^2), κ (eV Å^2) and η (eV Å^3).

	a	f_1	f_2	f_4	f_5	α	β	κ	η
MoS_2	3.18	2.14	1.24	-3.29	2.57	0.69	0.85	-2.0	3.5
$MoSe_2$	3.32	1.89	1.04	-2.94	2.17	0.49	0.58	-1.7	3.0
$MoTe_2$	3.55	1.5	0.85	-2.43	1.77	0.56	0.68	-1.8	3.0
WS_2	3.18	2.31	1.55	-3.82	3.22	1.29	1.71	-2.0	3.5
WSe_2	3.32	2.01	1.34	-3.53	2.77	1.13	1.47	-1.9	3.5
WTe_2	3.55	1.47	1.1	-2.99	2.29	1.32	1.75	-1.8	2.5
MoSSe	3.25	2.02	1.1	-3.10	2.29	0.64	0.80	-1.9	3.5
MoSeTe	3.43	1.7	0.87	-2.69	1.82	0.65	0.86	-1.8	2.5
WSSe	3.25	2.18	1.4	-3.68	2.90	1.24	1.68	-2.0	3.5
WSeTe	3.43	1.79	1.13	-3.32	2.35	1.25	1.78	-2.0	3.0

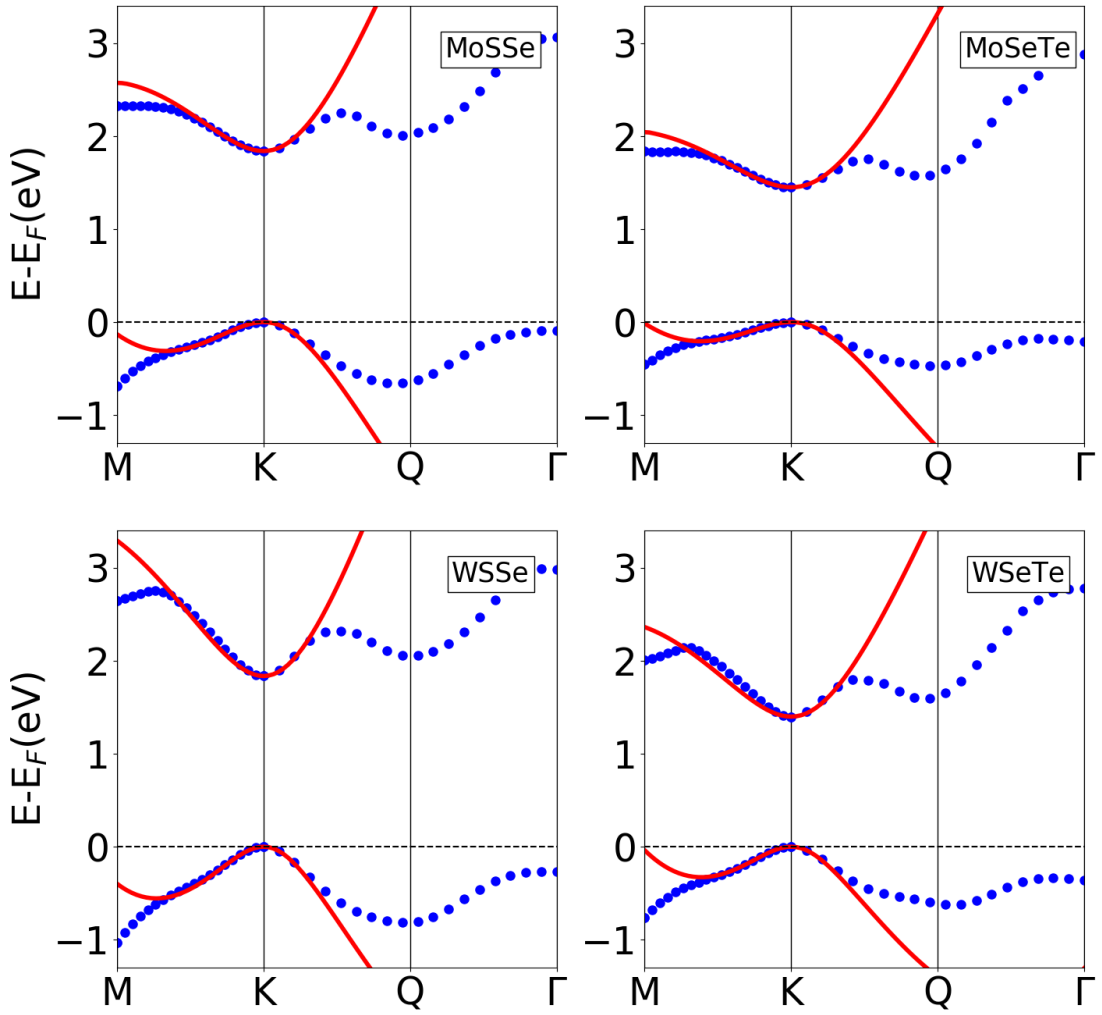

Figure 4: SOC band plots with $\mathbf{k}\cdot\mathbf{p}$ (solid lines) vs DFT(•) for spin down values.

$\mathbf{k}\cdot\mathbf{p}$ Results

The $\mathbf{k}\cdot\mathbf{p}$ method is proved to work well for TMDs in reproducing first-principles electronic structure around the CB and VB extrema.[48,57,58,61] Here, we demonstrate that this simple technique gives highly satisfactory results for direct band gap JTMDs: MoSSe, MoSeTe, WSSe, and WSeTe. The comparison with DFT including SOC are shown in Figures 4 and 5 for the spin down and up bands, respectively. The spinless cases are available in Figures S10 and S11. In extracting the associated $\mathbf{k}\cdot\mathbf{p}$ values, we followed the procedure as

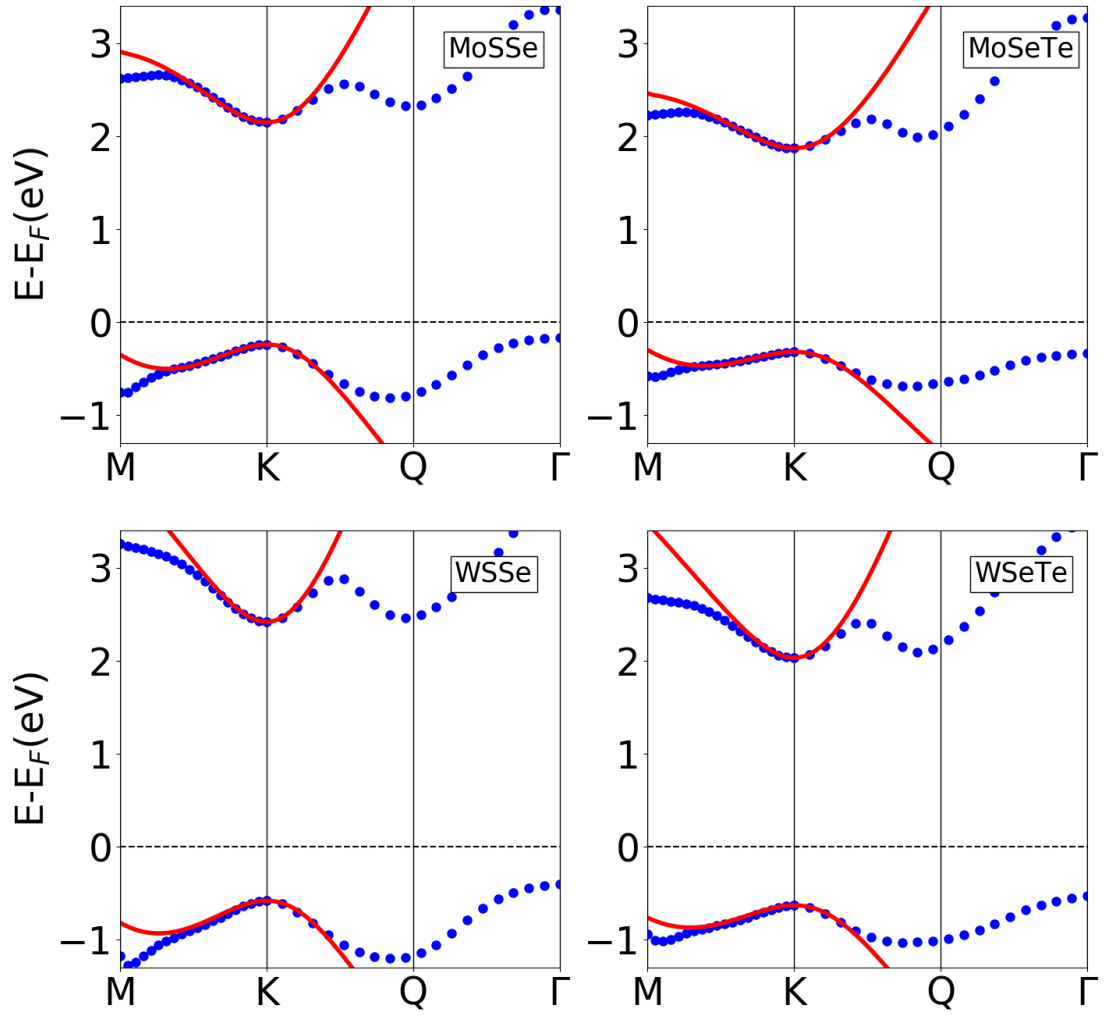

Figure 5: SOC band plots with $\mathbf{k}\cdot\mathbf{p}$ (solid lines) vs DFT(•) for spin up values.

described in the above section Parameter fitting expressions. For the unstrained band gap, E_g we used the hybrid DFT results tabulated in Table 1. The effective mass values needed for f_2, α, and β are available in Table S1.

The full listing of the spinless $\mathbf{k}\cdot\mathbf{p}$ parameters are given in Table 3 and the spinful ones in Table 4. We have a number of remarks on these. The trigonal warping as governed by the parameter κ is very effective in JTMDs, and it is in good agreement with DFT as shown in Figures 7 and 6 for the spin down and up bands, respectively. In these plots, it can be observed that in general the agreement extends to 200 meV away from

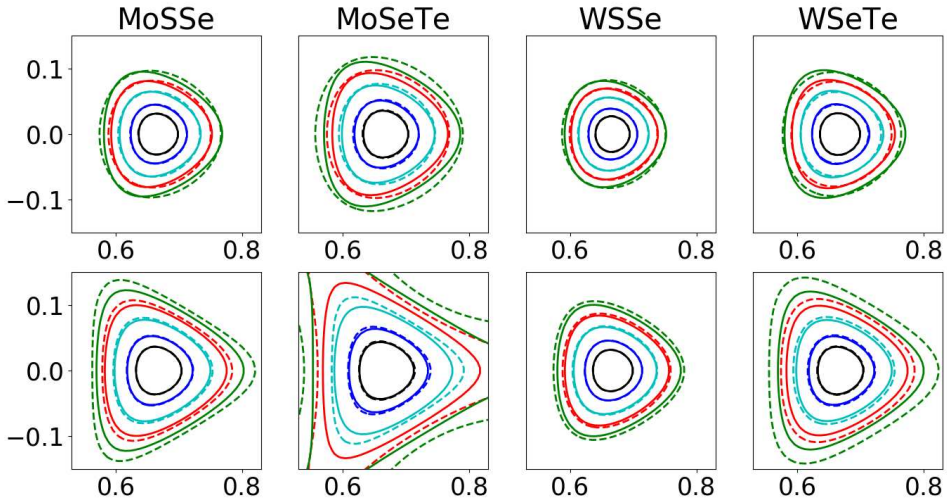

Figure 6: Isoenergy plots including SOC with $\mathbf{k} \cdot \mathbf{p}$ (solid lines) vs DFT(dashed lines) for spin up values (black, dark blue, light blue, red, and green lines correspond to the values 0.025, 0.05, 0.1, 0.15, and 0.2 eV).

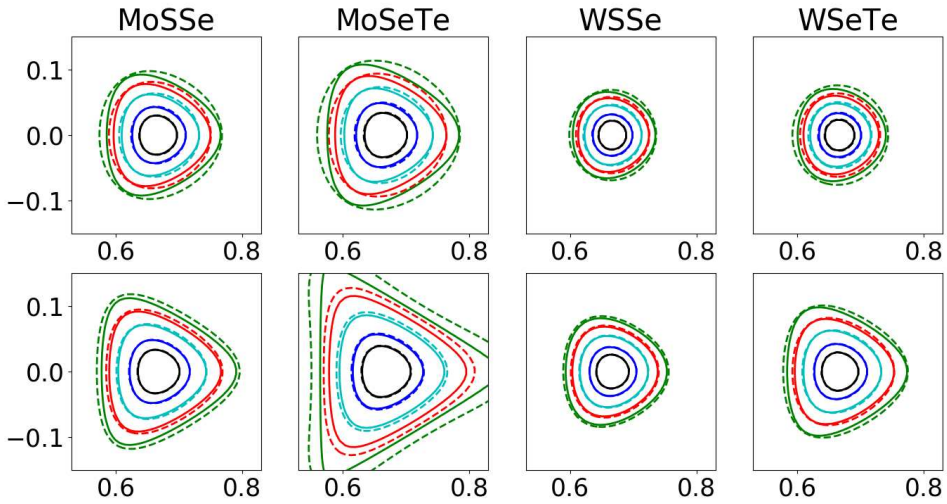

Figure 7: Isoenergy plots including SOC with $\mathbf{k} \cdot \mathbf{p}$ (solid lines) vs DFT(dashed lines) for spin down values (black, dark blue, light blue, red, and green lines correspond to the values 0.025, 0.05, 0.1, 0.15, and 0.2 eV).

the K point bandedge. For the cubic term $\widehat{H}_{\text{cub}}$ of the $\mathbf{k} \cdot \mathbf{p}$ Hamiltonian, keeping the suggestion that the diagonal cubic term is negligible in TMDs,[58] we only considered the off-diagonal form as in eq. (4). We fitted the corresponding coefficient η to achieve a wider range of agreement with the DFT, which is indeed so for the KM panel (see Figures 4 and 5). On the other hand, the performance for the $K\Gamma$ panel is less

satisfactory due to the additional valley at the so-called Q point. A fit that performs better is possible but at the expense of making the behavior semimetallic, which we opted to avoid.

The f_4 and f_5 parameters, as mentioned before, are taken to be spin-independent and found by using the biaxial and uniaxial strain results shown in the previous section. They are included in Table 3. Previously, these parameters were calculated for TMDs using PBE DFT.[61] In comparison, our f_4 parameters are somewhat larger as we used hybrid DFT band gaps, while our PBE results given in Table S6 of the Supporting Information agree with their values. For f_5, there is better match since the hybrid and PBE do not show much difference for shifts in the k space (see Table S6 of Supporting Information).

The Figures S10 to S17 contain further $\mathbf{k}\cdot\mathbf{p}$ vs DFT comparison plots for the remaining TMDs for both spinless and spinful cases.

Table 4: Spinful $\mathbf{k}\cdot\mathbf{p}$ parameters f_1 (eV), f_2 (eV), α (eV Å^2), β (eV Å^2), κ (eV Å^2) and η (eV Å^3).

	$f_1\uparrow$	$f_1\downarrow$	$f_2\uparrow$	$f_2\downarrow$	$\alpha\uparrow$	$\alpha\downarrow$	$\beta\uparrow$	$\beta\downarrow$	$\kappa\uparrow$	$\kappa\downarrow$	$\eta\uparrow$	$\eta\downarrow$
MoS_2	2.25	2.02	1.23	1.25	0.66	0.72	0.82	0.88	-2.2	-2.4	3.1	3.2
$MoSe_2$	2.04	1.72	1.04	1.03	0.5	0.51	0.6	0.61	-2.1	-2.5	3.0	3.3
$MoTe_2$	1.69	1.27	0.86	0.83	0.61	0.56	0.79	0.67	-2.0	-2.3	3.2	3.2
WS_2	2.54	1.99	1.5	1.57	1.19	1.4	1.62	1.82	-2.0	-2.0	3.0	3.0
WSe_2	2.26	1.64	1.29	1.34	1.05	1.21	1.42	1.51	-1.9	-1.9	3.0	3.2
WTe_2	1.8	1.07	1.1	1.09	1.28	1.41	1.83	1.76	-1.5	-1.6	3.3	3.3
MoSSe	2.15	1.87	1.1	1.1	0.71	0.62	0.93	0.76	-2.0	-2.3	3.0	3.0
MoSeTe	1.87	1.5	0.88	0.86	0.73	0.62	1.04	0.8	-1.9	-2.1	3.0	3.1
WSSe	2.42	1.84	1.33	1.42	0.97	1.52	1.3	2.06	-2.0	-1.9	3.0	3.0
WSeTe	2.03	1.41	1.06	1.14	0.68	1.81	0.87	2.72	-2.1	-2.0	3.0	2.8

Dichroism

Uniaxial Responsivity for Linear Dichroism at the K point.

An unstrained (J)TMD shows no LD at the K point due to symmetry[52] and for the same reason also under the biaxial strain. When the symmetry is lowered by uniaxial strain, a nonvanishing η_L appears at the K point which is studied in Figure 8 for the bandedge (spin-down) transition. Considering an uniaxial-only case (i.e., $\epsilon_{xx} = -\epsilon_{yy}, \epsilon_{xy} = 0$), η_L variation at the K point is close to a quadratic behavior up to $\epsilon_{xx} = 0.1$. The right panel of this Figure shows $\eta_L(\epsilon_{xx} = 0.1)$, where WTe_2 has the highest uniaxial responsivity to LD among all the studied materials. This result is preserved for the spinless calculation (see, Figure S18). At first thought, a large f_5 value would be primarily responsible for this behavior. But, as listed in Table 3,

WS_2 has about 50% higher f_5 value than WTe_2 even though it has a smaller responsivity than the latter. Analysis of the analytical form for η_L in eq. (38), as obtained for the symmetric part of the Hamiltonian H_{symm}, reveals that the small energy gap value also plays a crucial role in this outcome. According to Figure 8, the material with the least responsivity at the K point to uniaxial strain is MoSeTe.

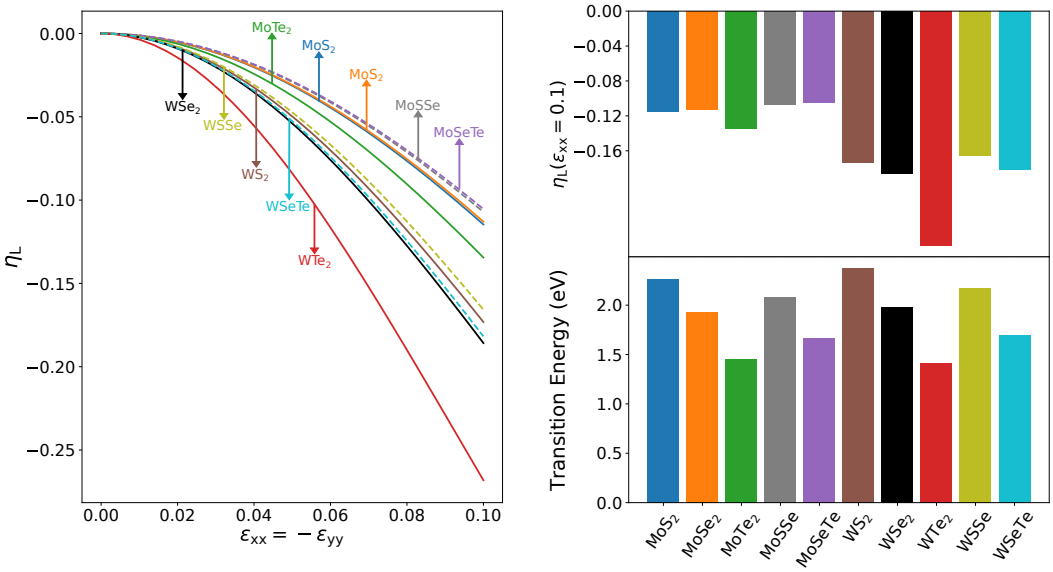

Figure 8: Variation of linear dichroism at the K point under uniaxial-only strain for the spin-down transition (left). $\eta_L(\epsilon_{xx} = 0.1)$ and transition energy values for the ten (J)TMDs (right).

Strain Dependence of Linear and Circular Dichroism at the K valley

Now, we turn to biaxial, uniaxial, and shear strain dependence of η_L and η_C over the K valley, again for an illumination with energy above the bandedge (spin-down) transition. We choose WSe_2, WTe_2, and their janus WSeTe as shown in Figure 9. The spinless case and the remaining materials are available in Figures S19, S22, S23, and S24. To gauge the effects of strain, in Figure 9(a) the unstrained $\eta_{L,C}$ are shown, which set the reference to demonstrate the deviation ($\Delta\eta_{L,C}$) at each k-point under biaxial-only (b), uniaxial-only (c), and shear-only (d) cases. A square area centered around the K point that spans $[-0.25, +0.25]$ in 1/Å along each direction is plotted. From a general perspective, among the 10 materials considered, the JTMDs display somewhat a larger variation in both η_L and η_C over the K valley (see also Figures S19, S22, S23, and S24). In line with the analytical expression in eq. (38), it is seen that $\Delta\eta_L$ and hence η_L change signs along the k_x $(\Gamma - K)$ for uniaxial strain and along the k_y $(\Gamma - M)$ for shear strain. These suggest a linear polarization-based measurement of these strain components in suspended (J)TMD membranes.

We can also investigate which terms in the $\mathbf{k}\cdot\mathbf{p}$ Hamiltonian are more influential in this general dichroic pattern. Comparing Figures 9 and 10, the most significant qualitative change is brought by the trigonal warping which is more pronounced for η_C. Furthermore, it was pointed out earlier that in contrast to gapped graphene, for TMDs the electron-hole asymmetry (eq. (2)) becomes important as it distinguishes the CB and VB Berry curvatures, thereby affecting also CD.[46] The remaining terms in the Hamiltonian introduce only quantitative changes for which we refer to Figures S20 and S21.

It would be very desirable to validate these results; however, so far there are few studies in this direction. Among them, ref[68] considers CD under 5% uniaxial strain where MoS_2 becomes indirect gap. On the other hand in this work, we refrained from exceeding about 2% strain with the intention to be confined in the direct band gap regime, with the exception of MS_2 and MSSe (M=Mo,W) which become indirect gap under lower values of uniaxial tensile strain. In the Supporting Information, the CD for unstrained MoS_2 is given in Figure S19 which compares well with ref.[74] The Figures S21 and S22 illustrate for WSe_2, WTe_2 and WSeTe the specific contributions to dichroism by the symmetric and also asymmetric terms in the Hamiltonian, respectively.

Conclusion

In this work, we focused on ten direct-band gap monolayer (J)TMDs and obtained spin-dependent $\mathbf{k}\cdot\mathbf{p}$ parameters including electron-hole asymmetry, trigonal warping, cubic, and biaxial or uniaxial strain effects. The fitting is based on our regular and hybrid DFT band structures in the presence of spin-orbit coupling and strain. A number of band properties calculated at the K valley indicate that the JTMD values show no marked deviation from those of the underlying pristine TMDs, in contrast to their reported superior piezoelectricity. We applied the $\mathbf{k}\cdot\mathbf{p}$ parameters in these materials to investigate the CD and LD around the K valley, where both of them display characteristic variations under biaxial, uniaxial, and shear strain components. Hence, a polarization-based absorption measurement can reveal the type of deformation in these monolayers. From the electronic structure point of view, the trigonal warping over the K valley is seen to be very influential on the CD. Finally, WTe_2 possesses the most pronounced uniaxial strain responsivity to LD, so that such membranes can be considered as strain tunable optical polarizers. In this respect the synthesis of this material becomes critical. According to one-step chemical vapor deposition growth of monolayer $WTe_{2x}S_{2(1-x)}$ alloys, when the Te concentration x is in the range of 0.4-0.6, a phase transition from the semiconducting 1H phase to the metallic to the 1T' phase is observed.[75] For this reason, the stability of the 1H WTe_2 under strain and/or different growth conditions warrants further investigation.

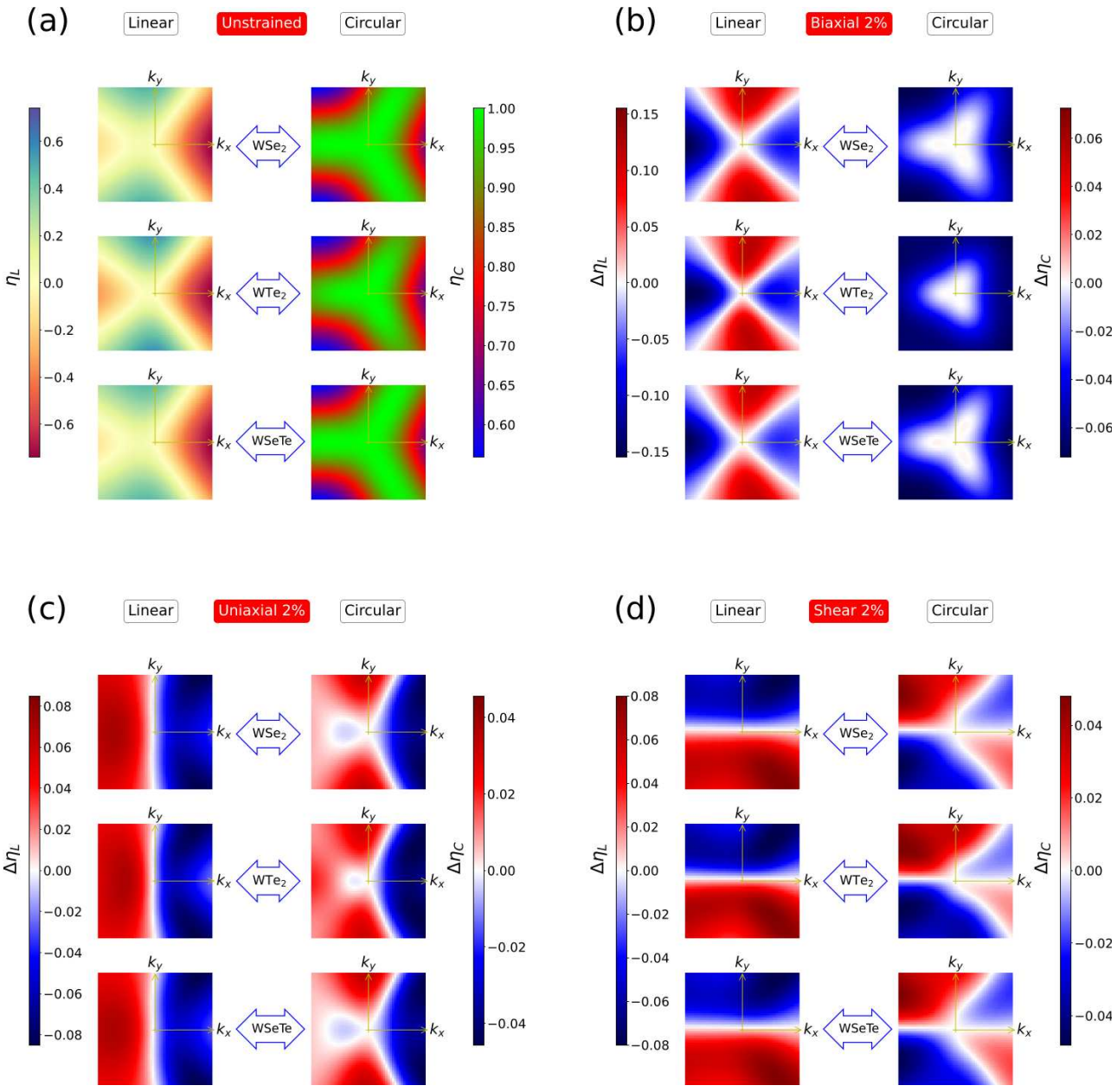

Figure 9: Variation of $\eta_{L,C}$ over the K valley for unstrained case (a), and its deviation from the unstrained reference ($\Delta\eta_{L,C}$) at each k-point for biaxial-only (b), uniaxial-only (c), and shear-only (d) cases for WSe_2, WTe_2, and their Janus WSeTe. A square region centered at the K point with $[-0.25, +0.25]$ in the $1/\text{Å}$ along each direction is shown. Above, the bandedge (spin-down) transition is considered.

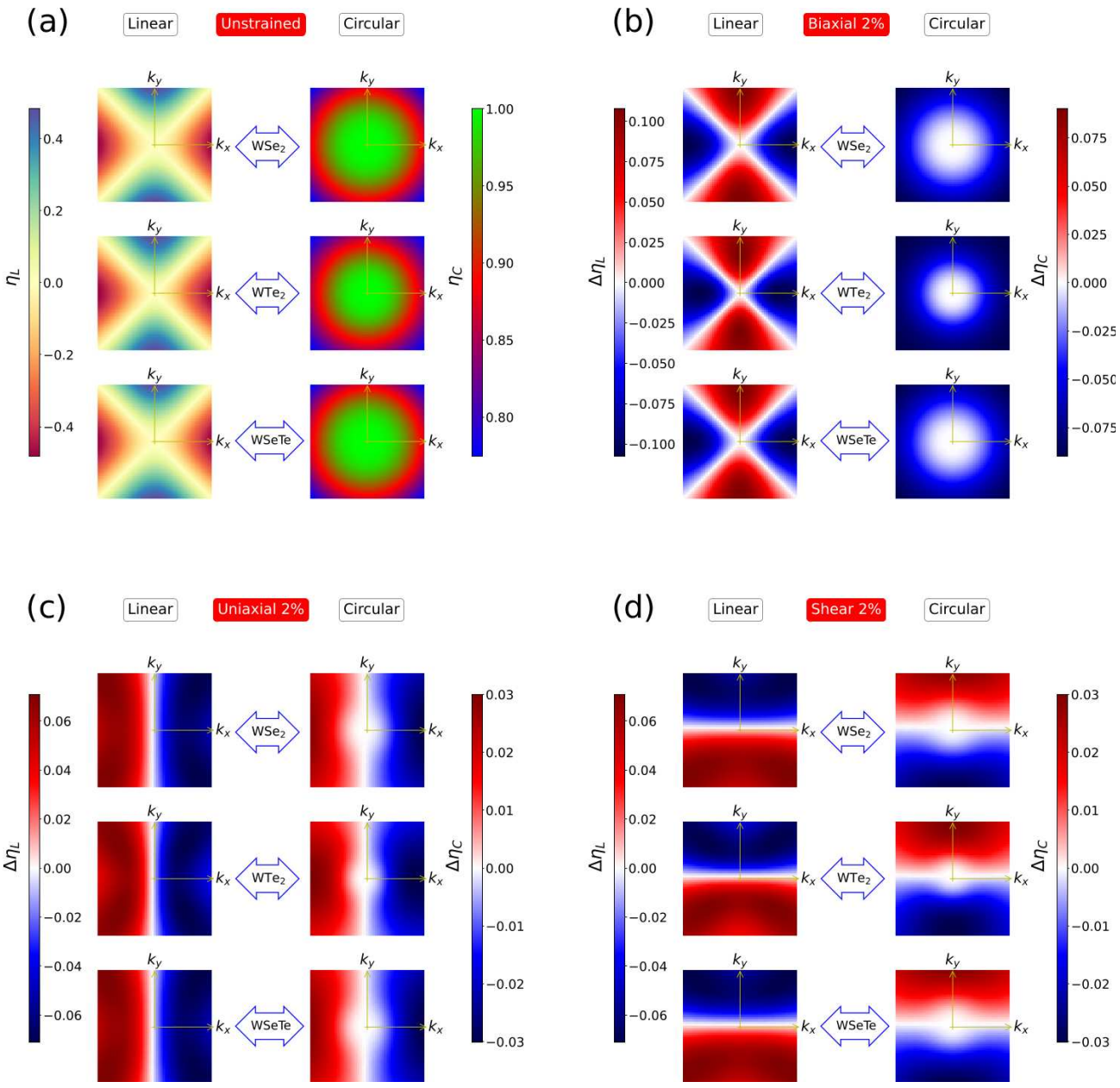

Figure 10: Same as the previous Figure, but without the trigonal warping term of the $\mathbf{k} \cdot \mathbf{p}$ Hamiltonian.

Acknowledgement

The numerical calculations reported in this paper were partially performed at TUBITAK ULAKBIM, High Performance and Grid Computing Center (TRUBA resources).

Supporting Information Available

DFT band structures of (J)TMDs with SOC and under biaxial/uniaxial strain, and comparisons with spinless/spinful $\mathbf{k} \cdot \mathbf{p}$, including the isoenergy plots at the K valley. Dichroism analysis for the spinless case and the effect of individual $\mathbf{k} \cdot \mathbf{p}$ Hamiltonian terms. Tables for the effective mass and band gaps under biaxial/uniaxial strain with PBE and HSE.

References

(1) Manzeli, S.; Ovchinnikov, D.; Pasquier, D.; Yazyev, O. V.; Kis, A. 2D transition metal dichalcogenides. *Nature Reviews Materials* **2017**, *2*, 17033.

(2) Radisavljevic, B.; Radenovic, A.; Brivio, J.; Giacometti, V.; Kis, A. Single-layer MoS_2 transistors. *Nature nanotechnology* **2011**, *6*, 147–150.

(3) Lee, C.; Yan, H.; Brus, L. E.; Heinz, T. F.; Hone, J.; Ryu, S. Anomalous lattice vibrations of single-and few-layer MoS_2. *ACS nano* **2010**, *4*, 2695–2700.

(4) Splendiani, A.; Sun, L.; Zhang, Y.; Li, T.; Kim, J.; Chim, C.-Y.; Galli, G.; Wang, F. Emerging photoluminescence in monolayer MoS_2. *Nano letters* **2010**, *10*, 1271–1275.

(5) Mak, K. F.; McGill, K. L.; Park, J.; McEuen, P. L. The valley Hall effect in MoS_2 transistors. *Science* **2014**, *344*, 1489–1492.

(6) Xu, X.; Yao, W.; Xiao, D.; Heinz, T. F. Spin and pseudospins in layered transition metal dichalcogenides. *Nature Physics* **2014**, *10*, 343–350.

(7) Wu, W.; Wang, L.; Li, Y.; Zhang, F.; Lin, L.; Niu, S.; Chenet, D.; Zhang, X.; Hao, Y.; Heinz, T. F., et al. Piezoelectricity of single-atomic-layer MoS_2 for energy conversion and piezotronics. *Nature* **2014**, *514*, 470–474.

(8) Lopez-Sanchez, O.; Lembke, D.; Kayci, M.; Radenovic, A.; Kis, A. Ultrasensitive photodetectors based on monolayer MoS_2. *Nature nanotechnology* **2013**, *8*, 497–501.

(9) Zhang, L.; Yang, Z.; Gong, T.; Pan, R.; Wang, H.; Guo, Z.; Zhang, H.; Fu, X. Recent advances in emerging Janus two-dimensional materials: from fundamental physics to device applications. *J. Mater. Chem. A* **2020**, *8*, 8813–8830.

(10) Wei, Y.; Tang, X.; Shang, J.; Ju, L.; Kou, L. Two-dimensional functional materials: from properties to potential applications. *International Journal of Smart and Nano Materials* **2020**, *11*, 247–264.

(11) Lu, A.-Y. et al. Janus monolayers of transition metal dichalcogenides. *Nature Nanotechnology* **2017**, *12*, 744–749.

(12) Zhang, J.; Jia, S.; Kholmanov, I.; Dong, L.; Er, D.; Chen, W.; Guo, H.; Jin, Z.; Shenoy, V. B.; Shi, L.; Lou, J. Janus Monolayer Transition-Metal Dichalcogenides. *ACS Nano* **2017**, *11*, 8192–8198, PMID: 28771310.

(13) Yagmurcukardes, M.; Sevik, C.; Peeters, F. M. Electronic, vibrational, elastic, and piezoelectric properties of monolayer Janus MoSTe phases: A first-principles study. *Phys. Rev. B* **2019**, *100*, 045415.

(14) Trivedi, D. B. et al. Room-Temperature Synthesis of 2D Janus Crystals and their Heterostructures. *Advanced Materials* **2020**, *32*, 2006320.

(15) Li, H.; Qin, Y.; Ko, B.; Trivedi, D. B.; Hajra, D.; Sayyad, M. Y.; Liu, L.; Shim, S.-H.; Zhuang, H.; Tongay, S. Anomalous Behavior of 2D Janus Excitonic Layers under Extreme Pressures. *Advanced Materials* **2020**, *32*, 2002401.

(16) Petrić, M. M.; Kremser, M.; Barbone, M.; Qin, Y.; Sayyad, Y.; Shen, Y.; Tongay, S.; Finley, J. J.; Botello-Méndez, A. R.; Müller, K. Raman spectrum of Janus transition metal dichalcogenide monolayers WSSe and MoSSe. *Phys. Rev. B* **2021**, *103*, 035414.

(17) Li, F.; Wei, W.; Huang, B.; Dai, Y. Excited-State Properties of Janus Transition-Metal Dichalcogenides. *The Journal of Physical Chemistry C* **2020**, *124*, 1667–1673.

(18) Chaurasiya, R.; Tyagi, S.; Singh, N.; Auluck, S.; Dixit, A. Enhancing thermoelectric properties of Janus WSSe monolayer by inducing strain mediated valley degeneracy. *Journal of Alloys and Compounds* **2021**, *855*, 157304.

(19) Hou, B.; Zhang, Y.; Zhang, H.; Shao, H.; Ma, C.; Zhang, X.; Chen, Y.; Xu, K.; Ni, G.; Zhu, H. Room Temperature Bound Excitons and Strain-Tunable Carrier Mobilities in Janus Monolayer Transition-Metal Dichalcogenides. *The Journal of Physical Chemistry Letters* **2020**, *11*, 3116–3128, PMID: 32220211.

(20) Guo, S.-D. Phonon transport in Janus monolayer MoSSe: a first-principles study. *Phys. Chem. Chem. Phys.* **2018**, *20*, 7236–7242.

(21) Cai, H.; Guo, Y.; Gao, H.; Guo, W. Tribo-piezoelectricity in Janus transition metal dichalcogenide bilayers: A first-principles study. *Nano Energy* **2019**, *56*, 33 – 39.

(22) Javvaji, B.; He, B.; Zhuang, X.; Park, H. S. High flexoelectric constants in Janus transition-metal dichalcogenides. *Phys. Rev. Materials* **2019**, *3*, 125402.

(23) Sun, Y.; Shuai, Z.; Wang, D. Janus monolayer of WSeTe, a new structural phase transition material driven by electrostatic gating. *Nanoscale* **2018**, *10*, 21629–21633.

(24) Long, C.; Dai, Y.; Gong, Z.-R.; Jin, H. Robust type-II band alignment in Janus-MoSSe bilayer with extremely long carrier lifetime induced by the intrinsic electric field. *Phys. Rev. B* **2019**, *99*, 115316.

(25) Ding, Y.; Yang, G.; Gu, Y.; Yu, Y.; Zhang, X.; Tang, X.; Lu, N.; Wang, Y.; Dai, Z.; Zhao, H.; Li, Y. First-Principles Predictions of Janus MoSSe and WSSe for FET Applications. *The Journal of Physical Chemistry C* **2020**, *124*, 21197–21206.

(26) Jena, N.; Dimple,; Ahammed, R.; Rawat, A.; Mohanta, M. K.; De Sarkar, A. Valley drift and valley current modulation in strained monolayer MoS_2. *Phys. Rev. B* **2019**, *100*, 165413.

(27) Ma, Y.; Kou, L.; Du, A.; Huang, B.; Dai, Y.; Heine, T. Conduction-band valley spin splitting in single-layer H-Tl_2O. *Phys. Rev. B* **2018**, *97*, 035444.

(28) Mohanta, M. K.; De Sarkar, A. Coupled spin and valley polarization in monolayer HfN_2 and valley-contrasting physics at the $HfN_2 - WSe_2$ interface. *Phys. Rev. B* **2020**, *102*, 125414.

(29) Idrees, M.; Din, H. U.; Ali, R.; Rehman, G.; Hussain, T.; Nguyen, C. V.; Ahmad, I.; Amin, B. Optoelectronic and solar cell applications of Janus monolayers and their van der Waals heterostructures. *Phys. Chem. Chem. Phys.* **2019**, *21*, 18612–18621.

(30) Mohanta, M. K.; De Sarkar, A. Interfacial hybridization of Janus MoSSe and BX (X= P, As) monolayers for ultrathin excitonic solar cells, nanopiezotronics and low-power memory devices. *Nanoscale* **2020**, *12*, 22645–22657.

(31) Kaur, S.; Kumar, A.; Srivastava, S.; Tankeshwar, K.; Pandey, R. Monolayer, bilayer, and heterostructures of green phosphorene for water splitting and photovoltaics. *The Journal of Physical Chemistry C* **2018**, *122*, 26032–26038.

(32) Mohanta, M. K.; Rawat, A.; Jena, N.; Dimple,; Ahammed, R.; De Sarkar, A. Interfacing Boron Monophosphide with Molybdenum Disulfide for an Ultrahigh Performance in Thermoelectrics, Two-Dimensional Excitonic Solar Cells, and Nanopiezotronics. *ACS Applied Materials & Interfaces* **2020**, *12*, 3114–3126, PMID: 31904214.

(33) Zhang, J.; Lang, X.; Zhu, Y.; Jiang, Q. Strain tuned InSe/MoS 2 bilayer van der Waals heterostructures for photovoltaics or photocatalysis. *Physical Chemistry Chemical Physics* **2018**, *20*, 17574–17582.

(34) Chaurasiya, R.; Dixit, A. Defect engineered MoSSe Janus monolayer as a promising two dimensional material for NO2 and NO gas sensing. *Applied Surface Science* **2019**, *490*, 204 – 219.

(35) Wang, D.; Lan, T.; Pan, J.; Liu, Z.; Yang, A.; Yang, M.; Chu, J.; Yuan, H.; Wang, X.; Li, Y.; Rong, M. Janus MoSSe monolayer: A highly strain-sensitive gas sensing material to detect SF6 decompositions. *Sensors and Actuators A: Physical* **2020**, *311*, 112049.

(36) Yang, X.-Y.; Hussain, T.; Wärnå, J. P. A.; Xu, Z.; Ahuja, R. Exploring Janus MoSSe monolayer as a workable media for SOF_6 decompositions sensing based on DFT calculations. *Computational Materials Science* **2021**, *186*, 109976.

(37) Chaurasiya, R.; Dixit, A. Ultrahigh sensitivity with excellent recovery time for NH3 and NO2 in pristine and defect mediated Janus WSSe monolayers. *Phys. Chem. Chem. Phys.* **2020**, *22*, 13903–13922.

(38) Ji, Y.; Yang, M.; Lin, H.; Hou, T.; Wang, L.; Li, Y.; Lee, S.-T. Janus Structures of Transition Metal Dichalcogenides as the Heterojunction Photocatalysts for Water Splitting. *The Journal of Physical Chemistry C* **2018**, *122*, 3123–3129.

(39) Wang, J.; Shu, H.; Zhao, T.; Liang, P.; Wang, N.; Cao, D.; Chen, X. Intriguing electronic and optical properties of two-dimensional Janus transition metal dichalcogenides. *Phys. Chem. Chem. Phys.* **2018**, *20*, 18571–18578.

(40) Rawat, A.; Mohanta, M. K.; Jena, N.; Dimple,; Ahammed, R.; De Sarkar, A. Nanoscale Interfaces of Janus Monolayers of Transition Metal Dichalcogenides for 2D Photovoltaic and Piezoelectric Applications. *The Journal of Physical Chemistry C* **2020**, *124*, 10385–10397.

(41) Xu, Y.; Yao, Y.; Yin, W.; Cao, J.; Chen, M.; Wei, X. Intrinsic defect engineered Janus MoSSe sheet as a promising photocatalyst for water splitting. *RSC Adv.* **2020**, *10*, 10816–10825.

(42) Ma, X.; Wu, X.; Wang, H.; Wang, Y. A Janus MoSSe monolayer: a potential wide solar-spectrum water-splitting photocatalyst with a low carrier recombination rate. *J. Mater. Chem. A* **2018**, *6*, 2295–2301.

(43) Ju, L.; Bie, M.; Tang, X.; Shang, J.; Kou, L. Janus WSSe Monolayer: An Excellent Photocatalyst for Overall Water Splitting. *ACS Applied Materials & Interfaces* **2020**, *12*, 29335–29343, PMID: 32519846.

(44) Zeng, H.; Dai, J.; Yao, W.; Xiao, D.; Cui, X. Valley polarization in MoS_2 monolayers by optical pumping. *Nature nanotechnology* **2012**, *7*, 490–493.

(45) Mak, K. F.; He, K.; Shan, J.; Heinz, T. F. Control of valley polarization in monolayer MoS_2 by optical helicity. *Nature nanotechnology* **2012**, *7*, 494–498.

(46) Cao, T.; Wang, G.; Han, W.; Ye, H.; Zhu, C.; Shi, J.; Niu, Q.; Tan, P.; Wang, E.; Liu, B.; Feng, J. Valley-selective circular dichroism of monolayer molybdenum disulphide. *Nature Communications* **2012**, *3*, 887.

(47) Sallen, G.; Bouet, L.; Marie, X.; Wang, G.; Zhu, C.; Han, W.; Lu, Y.; Tan, P.; Amand, T.; Liu, B., et al. Robust optical emission polarization in MoS_2 monolayers through selective valley excitation. *Physical Review B* **2012**, *86*, 081301.

(48) Aas, S.; Bulutay, C. Geometric band properties in strained monolayer transition metal dichalcogenides using simple band structures. *Journal of Applied Physics* **2019**, *126*, 115701.

(49) Srivastava, A.; Sidler, M.; Allain, A. V.; Lembke, D. S.; Kis, A.; Imamoğlu, A. Valley Zeeman effect in elementary optical excitations of monolayer WSe_2. *Nature Physics* **2015**, *11*, 141–147.

(50) Aivazian, G.; Gong, Z.; Jones, A. M.; Chu, R.-L.; Yan, J.; Mandrus, D. G.; Zhang, C.; Cobden, D.; Yao, W.; Xu, X. Magnetic control of valley pseudospin in monolayer WSe_2. *Nature Physics* **2015**, *11*, 148–152.

(51) Sengupta, P.; Pavlidis, D.; Shi, J. Optically adjustable valley Hall current in single-layer transition metal dichalcogenides. *Journal of Applied Physics* **2018**, *123*, 054301.

(52) Tong, L.; Duan, X.; Song, L.; Liu, T.; Ye, L.; Huang, X.; Wang, P.; Sun, Y.; He, X.; Zhang, L.; Xu, K.; Hu, W.; Xu, J.-B.; Zang, J.; Cheng, G. J. Artificial control of in-plane anisotropic photoelectricity in monolayer MoS_2. *Applied Materials Today* **2019**, *15*, 203 – 211.

(53) Kresse, G.; Furthmüller, J. Efficiency of ab-initio total energy calculations for metals and semiconductors using a plane-wave basis set. *Comput. Mater. Sci.* **1996**, *6*, 15–50.

(54) Kresse, G.; Joubert, D. From ultrasoft pseudopotentials to the projector augmented-wave method. *Phys. Rev. B* **1999**, *59*, 1758–1775.

(55) Heyd, J.; Scuseria, G. E.; Ernzerhof, M. Hybrid functionals based on a screened Coulomb potential. *J. Chem. Phys.* **2003**, *118*, 8207–8215.

(56) Voon, L. C. L. Y.; Willatzen, M. *The k.p method: electronic properties of semiconductors*; Springer Science & Business Media, 2009.

(57) Kormányos, A.; Zólyomi, V.; Drummond, N. D.; Rakyta, P.; Burkard, G.; Fal'ko, V. I. Monolayer MoS_2: Trigonal warping, the Γ valley, and spin-orbit coupling effects. *Phys. Rev. B* **2013**, *88*, 045416.

(58) Kormányos, A.; Burkard, G.; Gmitra, M.; Fabian, J.; Zólyomi, V.; Drummond, N. D.; Fal'ko, V. k· p theory for two-dimensional transition metal dichalcogenide semiconductors. *2D Materials* **2015**, *2*, 022001.

(59) Rostami, H.; Roldán, R.; Cappelluti, E.; Asgari, R.; Guinea, F. Theory of strain in single-layer transition metal dichalcogenides. *Phys. Rev. B* **2015**, *92*, 195402.

(60) Rybkovskiy, D. V.; C.Gerber, I.; Durnev, M. V. Atomically inspired k· p approach and valley Zeeman effect in transition metal dichalcogenide monolayers. *Phys. Rev. B* **2017**, *95*, 155406.

(61) Fang, S.; Carr, S.; Cazalilla, M. A.; Kaxiras, E. Electronic structure theory of strained two-dimensional materials with hexagonal symmetry. *Phys. Rev. B* **2018**, *98*, 075106.

(62) Roldán, R.; Castellanos-Gomez, A.; Cappelluti, E.; Guinea, F. Strain engineering in semiconducting two-dimensional crystals. *Journal of Physics: Condensed Matter* **2015**, *27*, 313201.

(63) Peter, Y.; Cardona, M. *Fundamentals of semiconductors: physics and materials properties*; Springer: Berlin and Heidelberg, 2010.

(64) Cardona, M.; Pollak, F. H. Energy-band structure of germanium and silicon: The k· p method. *Physical Review* **1966**, *142*, 530.

(65) Bulutay, C. Pseudopotential-Based Full Zone k.p Technique for Indirect Bandgap Semiconductors: Si, Ge, Diamond and SiC. *Turkish Journal of Physics* **2006**, *30*, 287–294.

(66) Perdew, J. P.; Burke, K.; Ernzerhof, M. Generalized Gradient Approximation Made Simple. *Phys. Rev. Lett.* **1996**, *77*, 3865–3868.

(67) Xiao, D.; Liu, G.-B.; Feng, W.; Xu, X.; Yao, W. Coupled Spin and Valley Physics in Monolayers of MoS_2 and Other Group-VI Dichalcogenides. *Phys. Rev. Lett.* **2012**, *108*, 196802.

(68) Wang, S.; Ukhtary, M. S.; Saito, R. Strain effect on circularly polarized electroluminescence in transition metal dichalcogenides. *Phys. Rev. Research* **2020**, *2*, 033340.

(69) Thanh, V. V.; Van, N. D.; Truong, D. V.; Saito, R.; Hung, N. T. First-principles study of mechanical, electronic and optical properties of Janus structure in transition metal dichalcogenides. *Applied Surface Science* **2020**, *526*, 146730.

(70) Guo, S.-D.; Dong, J. Biaxial strain tuned electronic structures and power factor in Janus transition metal dichalchogenide monolayers. *Semiconductor Science and Technology* **2018**, *33*, 085003.

(71) Shi, W.; Wang, Z. Mechanical and electronic properties of Janus monolayer transition metal dichalcogenides. *Journal of Physics: Condensed Matter* **2018**, *30*, 215301.

(72) Wang, Z. 2H $\rightarrow$ 1' phase transformation in Janus monolayer MoSSe and MoSTe: an efficient hole injection contact for 2H-MoS_2. *J. Mater. Chem. C* **2018**, *6*, 13000–13005.

(73) Xia, C.; Xiong, W.; Du, J.; Wang, T.; Peng, Y.; Li, J. Universality of electronic characteristics and photocatalyst applications in the two-dimensional Janus transition metal dichalcogenides. *Phys. Rev. B* **2018**, *98*, 165424.

(74) Rostami, H.; Volckaert, K.; Lanata, N.; Mahatha, S. K.; Sanders, C. E.; Bianchi, M.; Lizzit, D.; Bignardi, L.; Lizzit, S.; Miwa, J. A.; Balatsky, A. V.; Hofmann, P.; Ulstrup, S. Layer and orbital interference effects in photoemission from transition metal dichalcogenides. *Phys. Rev. B* **2019**, *100*, 235423.

(75) Tang, B.; Zhou, J.; Sun, P.; Wang, X.; Bai, L.; Dan, J.; Yang, J.; Zhou, K.; Zhao, X.; Pennycook, S. J., et al. Phase-controlled synthesis of monolayer ternary telluride with a random local displacement of tellurium atoms. *Advanced Materials* **2019**, *31*, 1900862.

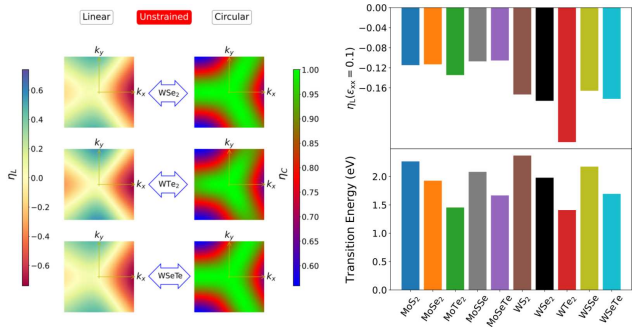

Figure 11: For Table of Contents Use Only.